Simulation and Design of $LiNbO_3$ Modulators With Switched Segmented Electrode Structure for High Bandwidth and Low Half-Wave Voltage

Hao Chen, Huangfan Wang, Feiwan Xie, Shaohua Yang, Huafeng Dong, Fugen Wu, and Wenyuan Liao

***Abstract*—A lithium niobate thin-film(LNTF) electro-optic modulator(EOM) with segmented electrode structure is investigated, and the influence of the modulator's structural configuration on its performance is achieved. In contrast to conventional couplers, the design incorporates a 2 × 2 S-shaped directional coupler. Our modulator achieves a bandwidth of nearly 110 GHz and a half-wave voltage of 1.45 V · cm. A comparative analysis between two configurations: one with SiO_2 cladding covering the entire surface and the other with coverage limited to the electrode gaps, which reveals the latter potential for enhancing device performance. The accuracy of the simulation results is substantiated through both software analysis and theoretical calculations. The simulation results provide valuable insights for the design of LNTF EOM, highlighting the efficacy of the proposed segmented electrode structure.**

***Index Terms*—LNTF EOM, Segmented electrode structure, s-shape directional coupler, electrode gap coverage, high bandwidth, low half-wave voltage.**

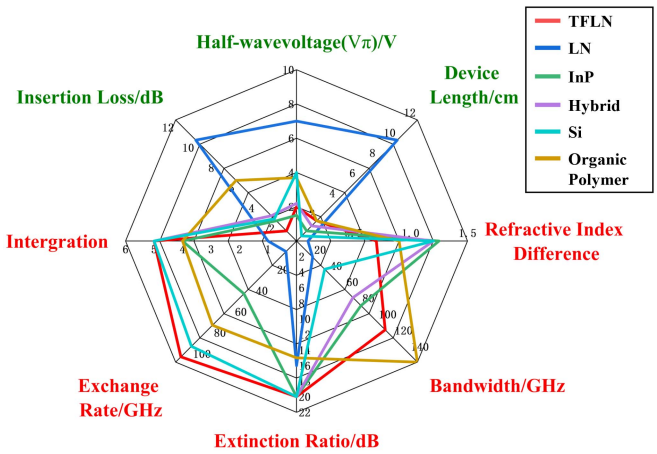

Fig. 1. EOMs performance comparison.

I. Introduction

EOMS are extensively employed in terrestrial and space optical communication systems. As the backbone network technology sinks, EOMs are being applied in shorter-distance scenarios like data centers and supercomputers. Optoelectronic devices embodying high performance, easy integration, low power consumption, and cost-effectiveness [1] are pivotal in propelling the progression of optical communication systems and large-scale photonic integrated systems. To meet the growing bandwidth demands in optical communications, researchers from diverse groups are actively exploring integrated EOMs with varied research priorities [2], [3], [4].

Manuscript received 22 November 2023; revised 28 December 2023; accepted 8 January 2024. Date of publication 11 January 2024; date of current version 27 February 2024. This work was supported in part by the National Natural Science Foundation of China under Grant 62127816 and in part by the Key Laboratory Project Foundation of China under Grant 6142806220101. *(Corresponding authors: Fugen Wu; Wenyuan Liao.)*

Hao Chen and Fugen Wu are with the School of Materials and Energy, Guangdong University of Technology, Guangzhou 510006, China (e-mail: wufg@gdut.edu.cn).

Huangfan Wang and Huafeng Dong are with the School of Physics and Optoelectronic Engineering, Guangdong University of Technology, Guangzhou 510006, China.

Feiwan Xie is with the Guangdong University of Technology, School of International Education, Guangzhou 511495, China.

Shaohua Yang and Wenyuan Liao are with the Reliability Physics and Application Technology of Electronic Component Key Laboratory, Guangzhou 511370, China (e-mail: wyliaophd@126.com).

Digital Object Identifier 10.1109/JPHOT.2024.3352697

Modulator performance optimization depends on device design and manufacturing while also taking into account retaining its inherent optoelectronic properties, such as low loss and low half-wave voltage (V_π), especially in pursuit of its bandwidth enhancement. In the context of traditional LN modulators founded on ion diffusion and proton exchange, a device length of 5 cm and a V_π of 3.5 V roughly represent theoretical thresholds [5]. Moreover, their stability beyond 40 GHz is limited. InP modulators can attain a bandwidth of 80 GHz and a V_π of 1.5 V [6], but challenges like a low extinction ratio and a slow exchange rate impede their practical viability. On the silicon platform or silicon-based integrated platform, certain research teams have successfully achieved over 110 GHz bandwidth and a 4 V V_π [7]. And another team has achieved a 70 GHz bandwidth with a half-wave voltage-length product ($V_\pi L$) of 2.2 V · cm [8]. While other platforms like polymers and plasmas have reported high-bandwidth modulators [9], [10], [11], this can sometimes require trade-offs that impact overall device stability, potentially leading to larger dimensions. LNTF offers a promising path. It preserves LN crystals' remarkable EO and nonlinear optical effects while leveraging ion cutting technology to boost the refractive index contrast between the waveguide and substrate structure [12]. This approach enhances voltage and bandwidth performance [13], [14], [15], [16]. Fig. 1 shows EOM performances across various platforms [17], [18], [19], [20]. A discernible trend is that LNTF exhibits potential for

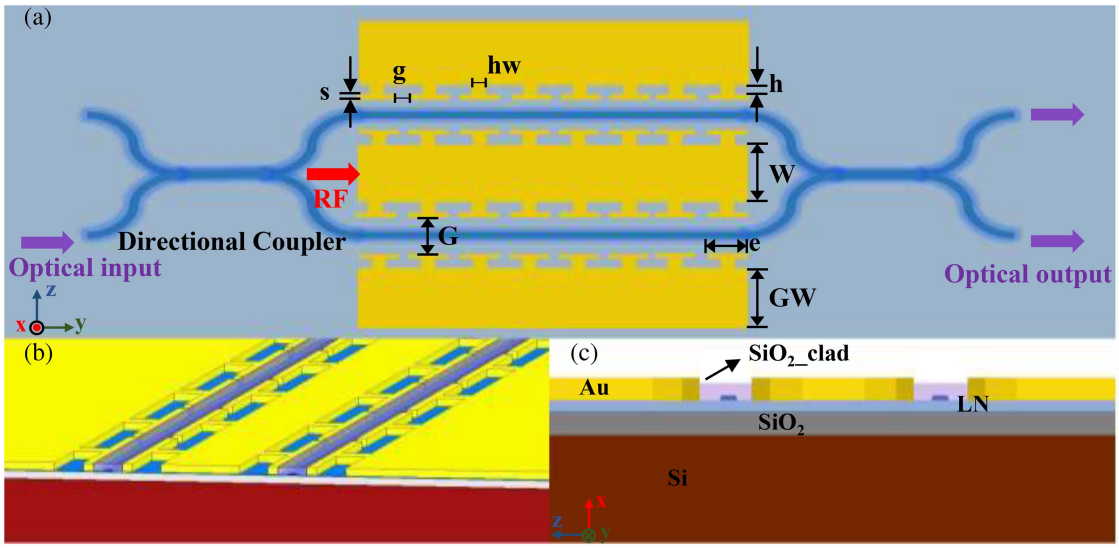

Fig. 2. Traveling-wave integrated lithium niobate (LN) modulator with segmented electrodes. (a) Schematic of the modulator design. (b) Diagram of the model built in the software. (c) Schematic cross-sectional view of the modulator. Design parameters (W, G, e, s, h, hw, g) = (16, 100, 45, 2, 6, 5, 5) μm.

both low-voltage operation and high bandwidth. X-cut LNTF EOMs commonly employ conventional rectangular Coplanar waveguides (CPW), but miniaturization and integration require narrow electrode gaps, leading to increased microwave losses. To address this, researchers propose segmented electrodes [21] to synchronize microwave transmission with light speed, enhancing modulation efficiency [22], [23], [24], [25]. A CPW with T-shaped internal slots achieves speed synchronization while maintaining optimal modulation efficiency [26]. An alternative approach utilizes a segmented CPW with reverse T-shaped epitaxy to achieve similar goals [21]. In conclusion, we found the following problems with the existence of LNTF EOMs:

- The structure of LNTF EOM is intricate. Layer dimensions notably impact modulator performance. Altered parameters may not consistently yield the desired outcomes. Optimal performance requires ongoing parameter research.
- Segmented electrode microstructures effectively widen bandwidth and microwave refractive index. However, the microstructure size's influence on device performance lacks study reporting.
- A top cladding of the LNTF waveguide [27], [28] minimizes losses from microwave transitions between low (air) and high (LN) dielectric materials and aids impedance matching. It may be possible to put cladding only within the electrode gap if the impedance is matched.
- The traditional Y-shaped branch requires a large bifurcation angle, so the distance between the two optical waveguides that need to be modulated cannot be further reduced. However, using a 2 $\times$ 2 curved directional coupler can solve this problem and get less loss with a suitable bend radius.

In this article, the LNTF EOM with a segmented electrode structure integrated with a directional coupler is designed, which can serve as an optical switch. Leveraging the collaborative optimization of COMSOL Multiphysics and Ansys HFSS simulation software, we achieve a $V_\pi L$ of 1.45 V $\cdot$ cm and a 3 dB bandwidth exceeding 110 GHz for the modulator. In addition, we delve into the analysis of the interplay among characteristic impedance, microwave refractive index, microwave loss, and the microelectrode structure. Simulation calculations verify the efficacy of this structure in enhancing the modulator's bandwidth while concurrently maintaining a lower V_π. This study offers a valuable reference for the performance optimization of LNTF modulators.

II. Modulator Design and Principal

The structural design of the modulator needs to be determined according to the actual application and requirements. In this article, our emphasis lies on devices that preserve lower voltages and can achieve bandwidths exceeding 100 GHz. The design of the device is shown in Fig. 2(a). The LNTF EOMs with switched segmented electrode structure are composed of two directional couplers and Mach-Zehnder interferometer (MZI). The input light is divided into two beams by the coupling effect of the directional coupler and enters the MZI. Under the traveling-wave electrode structure, the two beams of light propagate together with the microwave signal. Then, the application of electrical signals via GSG electrodes instigates opposing phase alterations within the two modulating arms, culminating in modulation (essentially a push-pull structure [29]). For LNTF EOMs, the applied voltage that causes π phase change is half-wave voltage, which can be expressed as:

$$V_\pi = \frac{\lambda G}{2n_e^3 \gamma_{33} L}, \tag{1}$$

where λ is the wavelength of light, G is the electrode gap, n_e is the effective refractive index of light, $\gamma_{33} = 31.2$ pm/V, L is the modulation length, and Γ is the electro-optic overlap integration factor [30]. Theoretically, achieving an exceptionally small V_π becomes feasible when the G is sufficiently minimized and

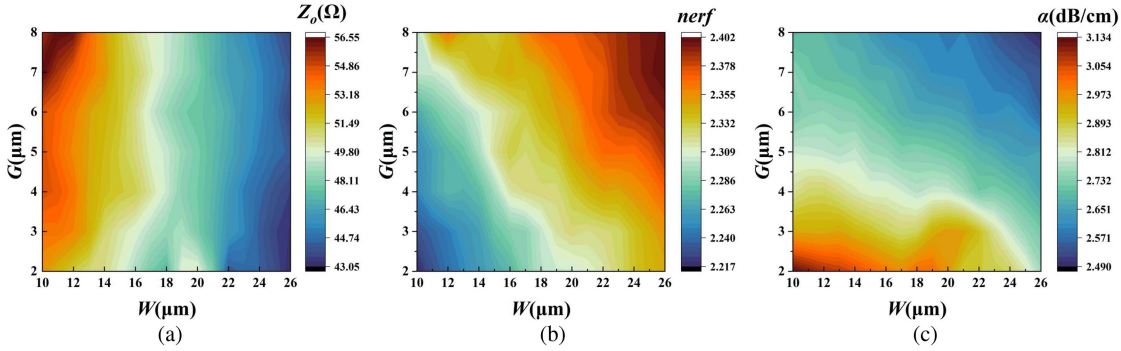

Fig. 3. Simulation results of structure and performance (a) the relationship between the Z_0 and the W and the G, (b) the relationship between the $nerf$ and the W and the G, and (c) the α and the relationship between W and the G.

the L is significantly extended. However, practical constraints emerge when the G becomes overly minute and the L becomes excessively elongated. These limitations result in an escalation of microwave loss, thereby impeding any further enhancement of the modulator's bandwidth. To put it differently, the pursuit of a wide bandwidth stands in contradiction to the aspiration for a low half-wave voltage. The performance of the bandwidth is limited by the following three factors [31]: (1) The loss of the microwave modulation signal and the attenuation of the driving voltage caused by the microwave loss. (2) The group velocity mismatch between the optical signal in the waveguide and the microwave signal in the transmission line leads to modulation obstruction. (3) The impedance mismatch with the external circuit leads to increased reflection and voltage loss. The design of the electrode structure directly determines the characteristic impedance (Z_0), microwave effective refractive index ($nerf$), and loss (α) of the modulator. Our design uses segmented T-shaped electrodes with periodic regularity [21]. The rules of segmented electrodes in this device can be expressed as:

$$X_n = L - n \times e - (n-1) \times g, \tag{2}$$

$$Y_n = L - (2n-1) \times e/2 - hw/2 - (\mathrm{n}-1) \times g, \tag{3}$$

where X_n is the center position of the segmented electrode connected to the core electrode, Y_n is the center position of the top of the T-shaped electrode. L is the total electrode length, n is the number of segments, e is the length of the unit electrode, hw is the width of the unit electrode, and g is the interval between the unit electrodes. (2) and (3) share factors with the same sign.

The T-shaped structure can effectively confine current to the channel region. These segments add somewhat to the capacitance and inductance per unit length. The capacitance blocks current flow across the intervening gap region, reducing ohmic losses. This eliminates the need to widen the electrode gap. Additionally, this arrangement doesn't require extra voltage to maintain light confinement capacity.

III. Simulation and Result Analysis

The design of the LNTF EOM encompasses both electrical and optical considerations. Electrical facets include GSG electrode dimensions (width and thickness), while optical considerations focus on waveguide etching depth. These factors collectively influence device performance. Once specific parameters are established, adjustments aligning with predetermined values enhance photonic and electronic performance. We conduct simulations to evaluate the performance of the modulator with a 1 cm electrode length. The model was built following the popular LNTF wafer specification with the following thicknesses from substrate to film: Si substrate with a thickness of 500 μm, a SiO_2 layer measuring 2 μm, and an LNTF layer with a depth of 600 μm. Additional etching and thinning steps are applied for design, and the model's details are shown in Fig. 2(b) and (c). This model is enclosed by air, and the bottom layer acts as a perfect match. During the performance investigation, precise parameters are established for each layer. Per traveling wave electrode theory, input impedance Z_{in} (usually 50 Ω) is expressed as:

$$Z_{in} = Z_0 \frac{Z_L + Z_0 \tanh(\gamma L)}{Z_0 + Z_L \tanh(\gamma L)}, \tag{4}$$

$$\gamma = \alpha + j\beta, \tag{5}$$

where Z_L is the load and source impedance. γ is the RF propagation constant in complex form. γ can be described as:

$$nerf = \frac{c}{verf} = \frac{c \times \beta}{2\pi f} = \frac{c \times Im(\gamma)}{2\pi f}, \tag{6}$$

Among them, c is the speed of light in vacuum, $verf$ is the microwave speed, f is the frequency, Im (γ) is the phase factor. When a beam of light and an RF signal start from the common origin of the CPW transmission line and the optical waveguide respectively. The phase of the microwave signal and the phase of the light wave in CPW are:

$$e^{-j\omega t} = e^{[(-j2\pi v/c)]z \times nerf}, \tag{7}$$

$$e^{-j\omega t} = e^{[(-j2\pi v/c)]z \times ne}, \tag{8}$$

Parameters such as layer thickness and $nerf$, while the etching depth of the optical waveguide governs the effective refractive index (ne). Consequently, for the purpose of achieving speed matching, we can achieve $nerf = ne$ by judiciously selecting suitable structural parameters. Fig. 3 visually shows the impact of electrode width and gap on EOM's electrical performance. Z_0 increases as the electrode gap (G) widens, while α decreases. A wider electrode (W) boosts capacitance per unit length while

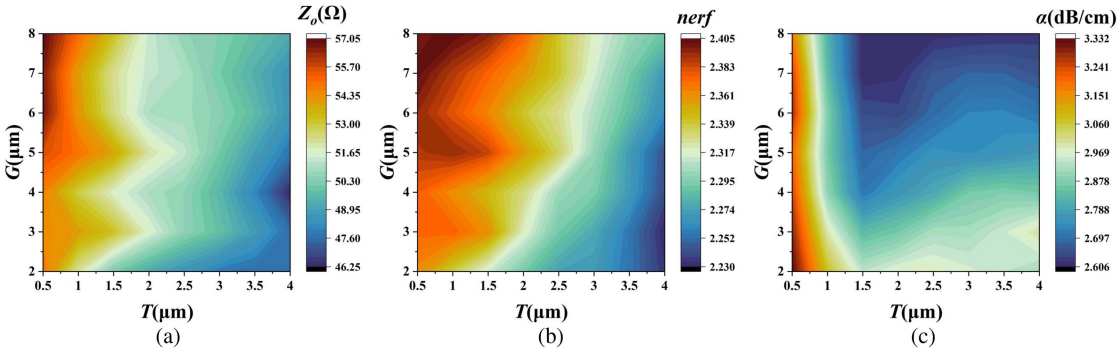

Fig. 4. Simulation results of structure and performance (a) the relationship between the Z_0 and the T and the G, (b) the relationship between the $nerf$ and the T and the G, and (c) the α and the relationship between the T and the G.

reducing inductance, thereby leading to a reduction in Z_0. In conventional rectangular electrode configurations, increasing electrode spacing reduces $nerf$ due to the greater proportion of decline in equivalent capacitance in comparison to the concurrent increase in equivalent inductance. However, by employing segmented electrodes, the $nerf$ decreases as electrode spacing narrows or displays slight fluctuations within a specific range. This characteristic proves advantageous for integration purposes. Opting for a segmented electrode configuration with a W of 16 μm and a G of 6 μm preliminarily achieves a Z_0 of 50 Ω along with lower losses.

The impact of electrode thickness (T) and G on the EOM's electrical performance is depicted in Fig. 4. It's evident that Z_0, $nerf$, and α decrease as T increases. With segmented electrodes, we also find that the nerf can be increased to the region of 2.1–2.4 (the $nerf$ of the traditional rectangular coplanar waveguide is generally 1.7–1.9). This outcome facilitates the synchronization of microwave phase velocity and optical group velocity (the ne is generally 2.2–2.3) because the microwave phase velocity is generally slower than the optical group velocity.

We present an innovative configuration wherein a covering layer is only added to the electrode gap. The incorporation of a SiO_2 covering layer proves effective in mitigating the losses stemming from the signal transition between materials with different dielectric constants. For T-shaped segmented electrodes, leveraging the derived capacitance resulting from lateral extension is crucial to impede current propagation. We speculate that adding the covering layer to the lateral epitaxial region's spacing might weaken current confinement efficacy. Consequently, we comparatively analyze both configurations, as shown in Fig. 5. Among them, Fig. 5(a) is a comparison diagram of the two structures. Fig. 5(b), (c) and (d) are the performance simulation results. Z_0 declines as G increases. Notably, the Z_0 of the selectively covered structure within the electrode gap is generally greater than that of the full coverage is a trend aligned with the relationship between Z_0 and G. Both nerf and α increase as G increases, with fully covered structure slightly surpassing α of structure with only electrode gap covering. Another important factor to consider is the optical metal absorption loss. We conducted a comparative analysis of the optical losses of the two structures under identical structural parameters, as depicted in Fig. 7(a). Under the same electrode

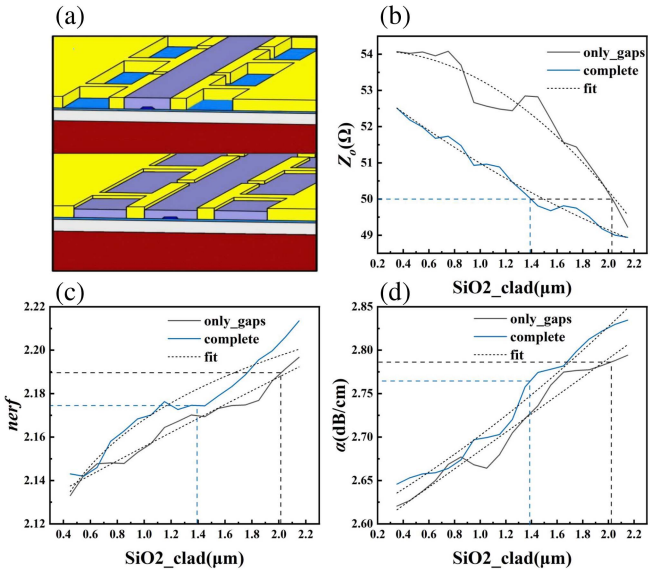

Fig. 5. Simulation results of modulator performance and SiO_2 cladding thickness (a) comparison of fully covered structure and only covered structure in the electrode gap, (b) the relationship between Z_0 and the thickness of the SiO_2 coating layer, (c) the relationship between the nerf and the thickness of the SiO_2 coating layer, and (d) the relationship between the α and the thickness of the SiO_2 coating layer.

gap, there is little difference in the optical mode loss of the two structures. Simultaneously, to visually represent the impact of metal proximity to the waveguide on the light mode, we simulated the mode analysis diagrams when G is 2 μm and G is 6 μm, as shown in Fig. 7(b). In the 2 μm cladding, an increase in electrode thickness resulted in heightened losses. Conversely, with a metal electrode thickness of 2 μm, augmenting the thickness of the cladding layer proved beneficial for reducing losses, as shown in Fig. 7(c) and (d). Hence, our configuration has potential to enhance modulator performance. In the modulation length of 1 cm, for the selected parameters of Z_0 at 50 Ω and $nerf$ within the range of 2.1–2.2, the electrode gap covering structure reaches about 2.0 μm thickness, while full coverage corresponds to roughly 1.4 μm. As a result, the respective volumes total 2.4 μm^3 and 2.73 μm^3.

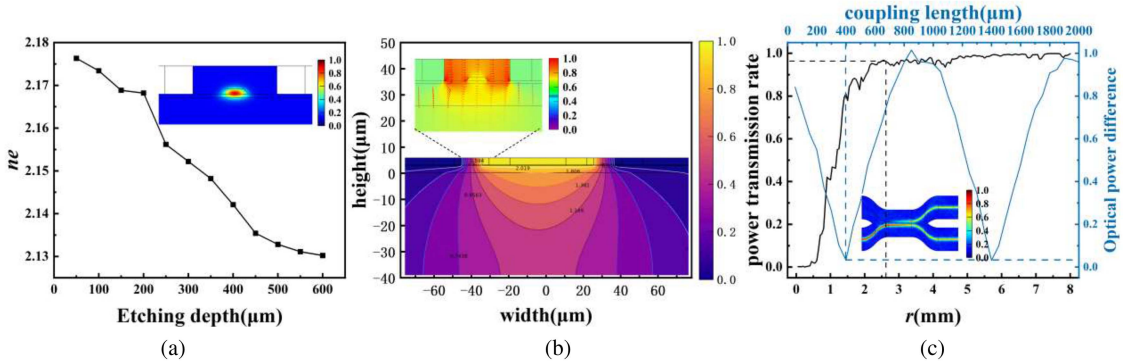

Fig. 6. Optical simulation of the LNTF EOM (a) the relationship between the ne and the etching depth of the waveguide, (b) the EX and ES of the modulator, and (c) the relationship between the light transmittance and the bending radius of the S-bend; the relationship between the optical power difference and the length of the directional coupler.

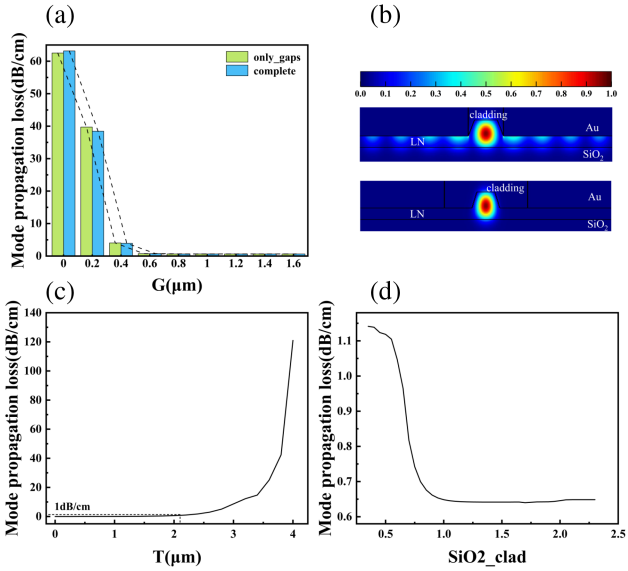

Fig. 7. (a) Optical losses of fully covered structure and only covered structure; (b) the mode analysis diagrams: G $= 2$ μm, G $= 6$ μm; (c) the metal absorption loss of the electrode thickness, G $= 6$ μm, SiO_2 $= 2$ μm; (d) the loss of the SiO_2 coating layer, G $= 6$ μm, T $= 2$ μm.

We utilized COMSOL Multiphysics for simulating optical pattern analysis, electrostatic field distribution (EX), and electric potential distribution (ES). Initially, we explore the connection between ne and the LNTF waveguide's etching depth (2 μm width for the waveguide's bottom). Fig. 6(a) shows a clear trend where greater etching depth corresponds to a lower ne. Here we select an etching depth of 250 nm for a ne of 2.156. Subsequently, we construct the x-cut section of the LNTF EOM and conduct an analysis of its ES and EX within the waveguide. As depicted in Fig. 6(b), the electric field mainly concentrates on both waveguide sides within the electrode gap. Moreover, the electric field's orientation within the waveguide region is parallel to the surface of the LNTF. Our device incorporates 2×2 double S-type directional couplers. This design necessitates the determination of two pivotal parameters. One is the bending radius (r), which demands careful selection to prevent excessive dispersion or confinement failure of light. The other is the directional coupling length. Maintaining optical power consistency between the upper and lower modulation arms prior to introducing an electrical signal is crucial. Illustrated in Fig. 6(c) is the relationship between r and light transmission, along with coupling length's impact on the optical power difference between arms. Evidently, the transmittance approaches its zenith and stabilizes when the r exceeds 2.6 mm. Simultaneously, at 400 μm coupling length, the optical power difference between arms minimizes.

IV. Performance and Calculation Verification

Finalizing the structural parameters of the LNTF EOM, we simulate and calculate its bandwidth and V_π. To assess the bandwidth, we initiated frequency sweeps through the software to ascertain its electrical-electrical (EE) response, as illustrated in Fig. 9. The EE S_{21} of -6.4 dB approaches 210 GHz, signifying an 3 dB EO bandwidth of approximately 105 GHz. When optical and microwave signals are perfectly matched, the 6.4 dB bandwidth of EE transmission is approximately equal to the 3 dB bandwidth of EO transmission. In pursuit of data accuracy validation, we further calculated bandwidth by employing the electro-optical response (EO-response) expression [32]. EO-response can be described as:

$$M(f) = 20log_{10}\left\{e^{-\frac{\alpha L}{2}}\left[\frac{sinh^2\left(\frac{\alpha L}{2}\right) + sin^2\left(\frac{bL}{2}\right)}{\left(\frac{\alpha L}{2}\right)^2 + \left(\frac{bL}{2}\right)^2}\right]^{\frac{1}{2}}\right\}, \tag{9}$$

Here α is the loss of the transmission line analyzed in the third part, b is the discrete parameter of light wave and microwave, and their frequency responses are shown in Fig. 8(a) and (b) respectively. The EO response is shown in Fig. 8(c), with a 3 dB bandwidth of 115 GHz, which is better than the software simulation results. We speculate that the error may be caused by the calculation accuracy of the software or the meshing.

For V_π, we also employe both software simulations and theoretical calculations for comparative validation. Upon the application of an electrical signal to the modulation region, modulated light experiences full transfer from one output port of the 2×2 switch MZM to the other output port. This voltage-port

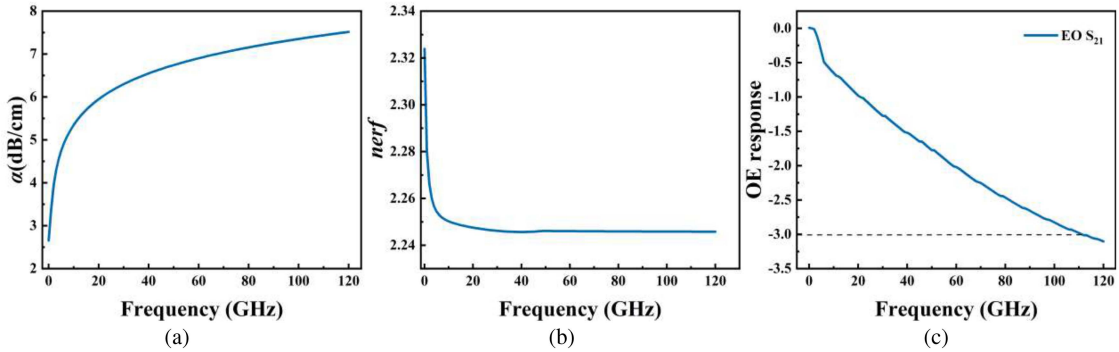

Fig. 8. Simulation results and theoretical calculation results of the modulator (a) frequency response of α, (b) frequency response of $nerf$, and (c) theoretical calculation of 3 dB bandwidth.

TABLE I
COMPARISON OF SIMULATED PERFORMANCE FOR VARIOUS ELECTRODE DESIGNS

Ref.	e (μm)	s (μm)	h (μm)	V_π	Bandwidth(GHz)	Zo (Ω)	$nerf$ (40 GHz)	α (dB/cm)(40GHz)	Optical Loss (dB/cm)
[19]	-	-	-	2.37	110	50.0	2.21	5.70	0.20
[28]	-	-	-	1.36	132	-	-	-	1.00
[29]	-	-	-	1.75	>40	-	-	-	0.70
[21]	45	2	3	1.30	>100	49.0	-	-	-
1	-	-	-	2.13	75	50.2	2.16	7.00	0.37
2	45	2	6	1.45	110	50.1	2.19	2.76	0.65
3	95	2	6	1.83	114	51.3	2.30	2.63	-
4	195	2	6	1.70	120	51.8	2.44	2.66	-
5	245	2	6	2.08	87	52.1	2.36	2.68	-
6	45	4	6	3.62	140	47.8	2.40	2.68	-
7	45	6	6	3.14	170	43.9	2.41	2.62	-
8	45	2	2	1.62	110	51.4	2.34	2.64	-

Note: Other parameters of the GSG electrode here remain the same; 1-8 are this work.
1: Non-segmented structure, W is equal to the S-pole body plus the lateral length of the T-shaped segmented structure
2-5: Based on an integer divisor of 1cm, e gradually increases 2, 6 and 7: s gradually increases

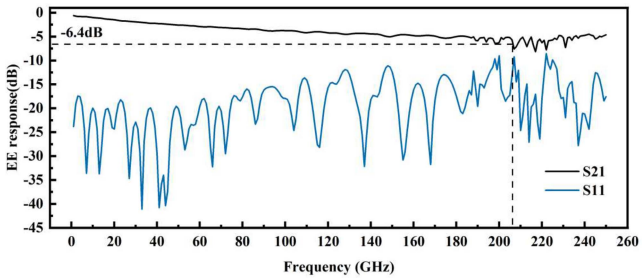

Fig. 9. Electrical-electrical (EE) response.

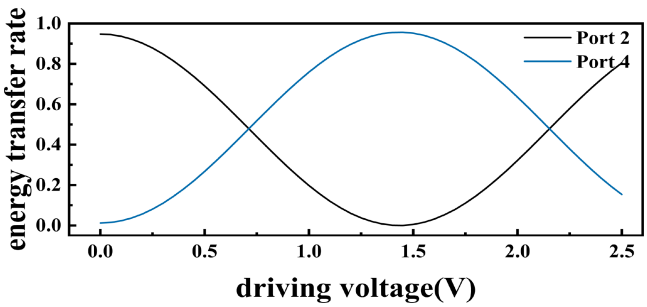

Fig. 10. Results of light energy distribution and voltage sweep.

energy transmittance correlation is depicted in Fig. 10. Evidently, with a voltage value of 1.45 V, complete energy transfer is achieved.

Furthermore, for a fixed modulation length and electrode gap, the V_π can be calculated using the electro-optic overlap integral factor, which can be described as:

$$Z_{in} = Z_0 \frac{Z_L + Z_0 \tanh(\gamma L)}{Z_0 + Z_L \tanh(\gamma L)}, \tag{10}$$

where $Eo(x, y)$ represents the optical mode field distribution, while $E(x, y)$ signifies the microwave field distribution. These values are attainable through optical mode analysis and electrostatic steady-state analysis, respectively. It's imperative to emphasize that the integration domain is half of the entire cross-section, that is, the photoelectric region corresponding to the waveguide within one of the modulation arms. Following calculation, the obtained value of Γ amounts to 0.445. Substituting this value into formula (1), the calculated V_π is determined as 1.55 V. This outcome exhibits a marginal difference of only 0.1 compared to the results obtained through voltage sweeping. The utilization of a segmented electrode configuration proves advantageous for maintaining a slender electrode gap. However, to achieve such a structure, it may occasionally require a broader S pole. This increased width has the potential to exceed the specified electrode gap width, resulting in an augmented separation between the two optical waveguides. As a consequence, there is a risk of an increased bending radius for a y-branch or other coupling structures. Such experimental may not align with our intended objectives. In consideration of these factors, we conducted a comparative analysis between devices devoid of

segmented structures and various sets of devices incorporating segmented configurations. The resultant characteristics are succinctly summarized in the accompanying Table. 1. In addition to the observed data in the table, which illustrates that increasing the length of e within a specific range enhances the bandwidth, we also observe that impedances slightly below 50 Ω yield a similar effect.

V. Discussion

Through an in-depth exploration of the correlation between device structure and performance, we have achieved remarkable improvements in both bandwidth and half-wave voltage characteristics. The precision of these outcomes has been substantiated through the verification of software simulations and theoretical calculations. However, due to the limitation of computer resources, we cannot explore the performance of other modulation lengths like 2 cm or the improvement of more structures. During our experimental endeavors, we discovered that the EE response performance tends to degrade beyond 210 GHz, with attempts to enhance it yielding limited success. Concurrently, we hold a strong interest in investigating whether other microstructure patterns of segmented electrodes can yield superior optimization effects. Moreover, while heterogeneously integrated waveguide structures show promise for bandwidth improvement, merging them with segmented configurations remains unexplored.

VI. Conclusion

In this study, a LNTF EOM with integrated segmented electrode structures and a 2 × 2 S-shaped directional coupler is designed. This configuration yielded an impressive bandwidth of nearly 110 GHz and achieved a $V_\pi L$ of 1.45 V · cm. Through software simulations, the impact of specific parameters related to the segmented electrode structure on the modulator's performance was thoroughly investigated. Meanwhile, it was observed that introducing SiO_2 cladding exclusively within the electrode gaps can improve the modulator's efficiency. The simulation outcomes were effectively corroborated through theoretical calculations, thereby validating the credibility of our findings. These results contribute vital insights for the advancement of modulator design, offering valuable reference points for future research endeavors in this field.

References

[1] M. Xu et al., "High-performance coherent optical modulators based on thin-film lithium niobate platform," *Nature Commun.*, vol. 11, no. 1, 2020, Art. no. 3911.

[2] M. Li, L. Wang, X. Li, X. Xiao, and S. Yu, "Silicon intensity Mach–Zehnder modulator for single lane 100 Gb/s applications," *Photon. Res.*, vol. 6, no. 2, pp. 109–116, 2018.

[3] C. Wang et al., "Integrated lithium niobate electro-optic modulators operating at CMOS-compatible voltages," *Nature*, vol. 562, no. 7725, pp. 101–104, 2018.

[4] P. O. Weigel et al., "Bonded thin film lithium niobate modulator on a silicon photonics platform exceeding 100 GHz 3-dB electrical modulation bandwidth," *Opt. Exp.*, vol. 26, no. 18, pp. 23728–23739, 2018.

[5] E. L. Wooten et al., "A review of lithium niobate modulators for fiber-optic communications systems," *IEEE J. Sel. Topics Quantum Electron.*, vol. 6, no. 1, pp. 69–82, Jan./Feb. 2000.

[6] Y. Ogiso et al., "80-GHz bandwidth and 1.5-VV π InP-based IQ modulator," *J. Lightw. Technol.*, vol. 38, no. 2, pp. 249–255, Jan. 2020.

[7] C. Han et al., "Slow-light silicon modulator with 110-GHz bandwidth," *Sci. Adv.*, vol. 9, no. 42, 2023, Art. no. eadi5339.

[8] M. He et al., "High-performance hybrid silicon and lithium niobate Mach–Zehnder modulators for 100 Gbit s- 1 and beyond," *Nature Photon.*, vol. 13, no. 5, pp. 359–364, 2019.

[9] S. Ummethala et al., "Hybrid electro-optic modulator combining silicon photonic slot waveguides with high-k radio-frequency slotlines," *Optica*, vol. 8, no. 4, pp. 511–519, 2021.

[10] S. Ummethala et al., "Capacitively coupled silicon-organic hybrid modulator for 200 Gbit/s PAM-4 signaling," in *Proc. CLEO: QELS_Fundamental Sci.*, 2019, Paper JTh5B.2.

[11] M. Burla et al., "500 Ghz plasmonic Mach-Zehnder modulator enabling sub-THz microwave photonics," *Apl Photon.*, vol. 4, no. 5, 2019, Art. no. 056106.

[12] G. Poberaj, M. Koechlin, F. Sulser, A. Guarino, J. Hajfler, and P. Günter, "Ion-sliced lithium niobate thin films for active photonic devices," *Opt. Mater.*, vol. 31, no. 7, pp. 1054–1058, 2009.

[13] J. Jian et al., "High modulation efficiency lithium niobate Michelson interferometer modulator," *Opt. Exp.*, vol. 27, no. 13, pp. 18731–18739, 2019.

[14] A. J. Mercante, S. Shi, P. Yao, L. Xie, R. M. Weikle, and D. W. Prather, "Thin film lithium niobate electro-optic modulator with terahertz operating bandwidth," *Opt. Exp.*, vol. 26, no. 11, pp. 14810–14816, 2018.

[15] A. Honardoost, F. A. Juneghani, R. Safian, and S. Fathpour, "Towards subterahertz bandwidth ultracompact lithium niobate electrooptic modulators," *Opt. Exp.*, vol. 27, no. 5, pp. 6495–6501, 2019.

[16] X. Liu et al., "Wideband thin-film lithium niobate modulator with low half-wave-voltage length product," *Chin. Opt. Lett.*, vol. 19, no. 6, 2021, Art. no. 060016.

[17] M. Zhang, C. Wang, P. Kharel, D. Zhu, and M. Lonvčar, "Integrated lithium niobate electro-optic modulators: When performance meets scalability," *Optica*, vol. 8, no. 5, pp. 652–667, 2021.

[18] M. Stepanenko, I. Yunusov, V. Arykov, P. Troyan, and Y. Zhidik, "Multiparameter optimization of an InP electro-optic modulator," *Symmetry*, vol. 12, no. 11, 2020, Art. no. 1920.

[19] F. Yang et al., "Monolithic thin film lithium niobate electro-optic modulator with over 110 GHz bandwidth," *Chin. Opt. Lett.*, vol. 20, no. 2, 2022, Art. no. 022502.

[20] Y. Zhu et al., "Toward single lane 200G optical interconnects with silicon photonic modulator," *J. Lightw. Technol.*, vol. 38, no. 1, pp. 67–74, 2020.

[21] P. Kharel, C. Reimer, K. Luke, L. He, and M. Zhang, "Breaking voltage–bandwidth limits in integrated lithium niobate modulators using micro-structured electrodes," *Optica*, vol. 8, no. 3, pp. 357–363, 2021.

[22] G. Li, T. Mason, and P. Yu, "Analysis of segmented traveling-wave optical modulators," *J. Lightw. Technol.*, vol. 22, no. 7, 2004, Art. no. 1789.

[23] J. Shin, S. R. Sakamoto, and N. Dagli, "Conductor loss of capacitively loaded slow wave electrodes for high-speed photonic devices," *J. Lightw. Technol.*, vol. 29, no. 1, pp. 48–52, Jan. 2011.

[24] R. Ding et al., "High-speed silicon modulator with slow-wave electrodes and fully independent differential drive," *J. Lightw. Technol.*, vol. 32, no. 12, pp. 2240–2247, 2014.

[25] X. Liu et al., "Low half-wave-voltage thin film $LiNbO_3$ electro-optic modulator based on a compact electrode structure," in *Proc. Asia Commun. Photon. Conf.*, 2020, pp. M4A–144.

[26] X. Huang et al., "Advanced electrode design for low-voltage high-speed thin-film lithium niobate modulators," *IEEE Photon. J.*, vol. 13, no. 2, Apr. 2021, Art. no. 7900609.

[27] A. Alam and J. Aitchison, "Low half-wave-voltage lithium niobate modulator using high-K dielectric material cladding," in *Proc. Opt. Dev. Mater. Sol. Energy Solid-state Lighting*, 2022, pp. JTu2A–9.

[28] A. S. Alam and J. S. Aitchison, "Optimization of a broadband lithium niobate-barium titanate hybrid modulator with low half-wave-voltage-length product," *IEEE Photon. J.*, vol. 15, no. 6, pp. 1–7, Dec. 2023.

[29] Y. Liu, H. Li, J. Liu, S. Tan, Q. Lu, and W. Guo, "Low v πthin-film lithium niobate modulator fabricated with photolithography," *Opt. Exp.*, vol. 29, no. 5, pp. 6320–6329, 2021.

[30] D.-G. Sun, Z. Liu, Y. Huang, S.-T. Ho, D. J. Towner, and B. W. Wessels, "Performance simulation for ferroelectric thin-film based waveguide electro-optic modulators," *Opt. Commun.*, vol. 255, no. 4/6, pp. 319–330, 2005.

[31] X. Li et al., "Heterogeneously integrated thin-film lithium niobate electro-optic modulator based on slot structure," *Curr. Opt. Photon.*, vol. 6, no. 3, pp. 323–331, 2022.

[32] S. K. Korotky, "Lithium niobate integrated optics: Selected contemporary devices and system applications," *Optical Fiber Telecommun. III CH*, vol. 9, p. 377, 1997.